MDPI

Article

Electron Beam Additive Manufacturing of SS316L with a Stochastic Scan Strategy: Microstructure, Texture Evolution, and Mechanical Properties

K. N. Chaithanya Kumar [1], Shashank Sharma [1,2,3], Madhavan Radhakrishnan [1,2], Rohit Randhavan [1,2], Krishna Kamlesh Verma [1], Shelden Dowden [1], Zane Weldon Hughes [1], Rajarshi Banerjee [1,2] and Narendra B. Dahotre [1,2,*]

1   Center for Agile and Adaptive Additive Manufacturing, University of North Texas, Denton, TX 76207, USA; kn.chaithanyakumar@unt.edu (K.N.C.K.); shashank.sharma@unt.edu (S.S.); madhavan.radhakrishnan@unt.edu (M.R.); rohitrandhavan@my.unt.edu (R.R.); krishna.verma@unt.edu (K.K.V.); shelden.dowden@unt.edu (S.D.); zane.hughes@unt.edu (Z.W.H.); raj.banerjee@unt.edu (R.B.)
2   Department of Materials Science & Engineering, University of North Texas, Denton, TX 76207, USA
3   Department of Mechanical Engineering, University of North Texas, Denton, TX 76207, USA
*   Correspondence: narendra.dahotre@unt.edu; Tel.: +1-(940)-369-7678

Abstract: This study examines the microstructure, crystallographic texture evolution, and mechanical properties of stainless steel 316L fabricated through electron beam melting using a stochastic scan strategy at a preheat temperature of 1123 K. X-ray diffraction confirmed the presence of a pure austenitic phase in the fabricated material. Equiaxed cellular structures were observed in the center of the melt pool regions and elongated cellular structures observed at the melt pool overlap regions. A finite element-based numerical model was employed to estimate the thermal gradients and solidification rates within the melt pool of an electron beam spot. Microstructural analysis indicated a generation of columnar grains from the bottom to the top of the build owing to high thermal gradients. A crystallographic texture investigation showed a generation of strong <110> fiber texture along the build direction of the material and reported that the stress distributions within the melt pool led to a strong crystallographic texture driven by the stress evolution observed from thermokinetic computational modelling of the electron beam-melting process. Mechanical properties were assessed using profilometry-based indentation plastometry, demonstrating strain hardening at a high temperature of 773 K.

Keywords: additive manufacturing; electron beam melting; stainless steel; microstructure; modelling; tensile properties

1. Introduction

Additive manufacturing (AM) technologies have revolutionized the production of components with reduced processing steps and complex components by offering enhanced design flexibility, material efficiency, and shortened production cycles [1–4]. Among the various AM techniques, electron beam melting (EBM) has emerged as one of the most advantageous processes, particularly for processing metallic and intermetallic materials, due to its unique operating environment (a vacuum chamber and preheated substrate) and processing strategies [5]. The EBM in a vacuum chamber significantly reduces oxidation risks, making it ideal for reactive materials like titanium alloys [6] and stainless steel [7]. Furthermore, the lower cooling rates of EBM, along with the maintenance of high temperatures throughout the build, help minimize thermal gradients, thereby reducing residual stresses, warping, and distortion, which are often observed in other AM processes such as laser-based powder bed fusion (PBF) or laser-based direct energy deposition (DED) [8,9].

Stainless steel 316L (SS316L) is known for its corrosion resistance [10] and mechanical strength [11], making it ideal for applications in the aerospace, biomedical, and industrial sectors [12,13]. Oxidation is hard to avoid in the fabrication of stainless steels, with Si–Cr–Mn oxides formed in laser-based additive manufacturing [7] as it is operated in an inter-gas atmosphere. On the contrary, the EBM process operated in a vacuum with a higher build temperature would avoid oxidation, prevent build failure caused by the charging of electrons [14,15], reduce the residual stresses, and increase the yield strength in the material [16,17]. During the EBM process, a low preheat temperature leads to faster cooling rates with increased residual stress in the material, which can cause material distortion or delamination of layers, limiting the component applications without further thermal processing [18]. A very high preheat temperature with prolonged heating can cause a reduction in the precision and accuracy of components made using the EBM process [19,20]. Additionally, excessively high preheat temperatures can promote grain growth, leading to coarser grains and, consequently, reducing the mechanical performance of the final component [21]. The scanning strategy used in EBM is equally important in determining the microstructure of the fabricated parts. The selection of the scan strategy directly influences the thermal history during solidification, affecting the grain size and morphology and influencing the overall part performance. Among linear scan, ordered spot scan, and stochastic spot scan strategies used in the fabrication of Ti64 at a build temperature of 743 K using EBM, the grain size was considerably reduced when the spot scan strategy was employed due to a faster cooling rate with multiple thermal gyrations within the solid phase formed from liquid [22]. Similar observations of reduction in grain sizes were reported when printed using spot scan strategy during EBM of IN718 at a bed temperature of 1323 K [23]. Lee et al. investigated the variations in thermal gradients and solidification rates with varying scan strategies in the EBM process and reported that there are relatively lower thermal gradients and solidification rates in the materials affecting the microstructural evolution while using a randomly ordered spot strategy compared to ordered spot and raster scan strategies [24]; the preheating of the substate in addition to use of these scan strategies during processing further reduces the thermal gradients and solidification rates considerably in the material [23]. Such changes in lower solidification rates, in addition to a higher melt pool area using the spot melting strategy, assisted in the mitigation of gas porosity [25]. The combined effect of the preheating, spatial arrangement of electron beam (e-beam) spots within a layer and the stochastic temporal order of melting can control the thermal accumulation aspect, which might be significant for thermal management required in e-beam printing of difficult-to-melt refractory metals such as tungsten [26].

Hence, process parameters in EBM, such as scanning strategies and preheat temperatures, have a profound influence on microstructural development, particularly on grain size and morphology, which directly affect the mechanical properties of the final parts. In the case of SS316L, investigating the combined effect of a high preheat temperature and stochastic scanning strategy is essential to understanding how these factors work together on the microstructure evolution and mechanical properties. It has not yet been extensively studied under these specific conditions in SS316L. Thus, the present study focused on understanding the morphological and textural evolution correlating with thermo-mechanical stress evolution using computational modeling and mechanical properties of electron beam melted SS316L employing a stochastic scan strategy with a preheat temperature of 1123 K, providing valuable insights for future applications.

2. Materials and Methods

2.1. The EBM® Process

SS316L powders used for the EBM process were supplied by Carpenter Powder Products AB (Carpenter Powder Products AB, Västerås, Sweden) of MICRO-MELT® 316L grade. The Micrograph in Figure 1a shows that these powders are of a spherical morphology. The size of these particles was measured using a Microtrac™ S3500 laser diffraction analyzer

(Microtrac, Inc., Montgomeryville and York, PA, USA) (Figure 1b). The component fabrication was performed using a Freemelt® One PBF-EB machine (Freemelt AB, Molndal, Sweden). The beam accelerating voltage was set at 60 kV, and a beam current of 11 mA was applied. This study implemented a stochastic scan strategy (PixelMelt® (version 1, Freemelt AB, Mölndal, Sweden)), in Freemelt® (Freemelt AB, Mölndal, Sweden), utilizing a calibrated electron beam spot size of 200 μm with a beam dwell time of 0.25 ms at a preheat temperature 1123 K. The stochastic point scan strategy, depicted in Figure 2, involved random point-by-point scanning of the area within each layer, with no intra-layer rotation. The distance between consecutive electron beam spots was maintained at 350 μm. The positioning of e-beam spots in one layer aligns with those in other layers of the component. Nevertheless, the order of the melting of spots in the bottom layer differs from that in the top layer, exhibiting stochastic variation throughout all layers of the component.

(**a**)   (**b**)
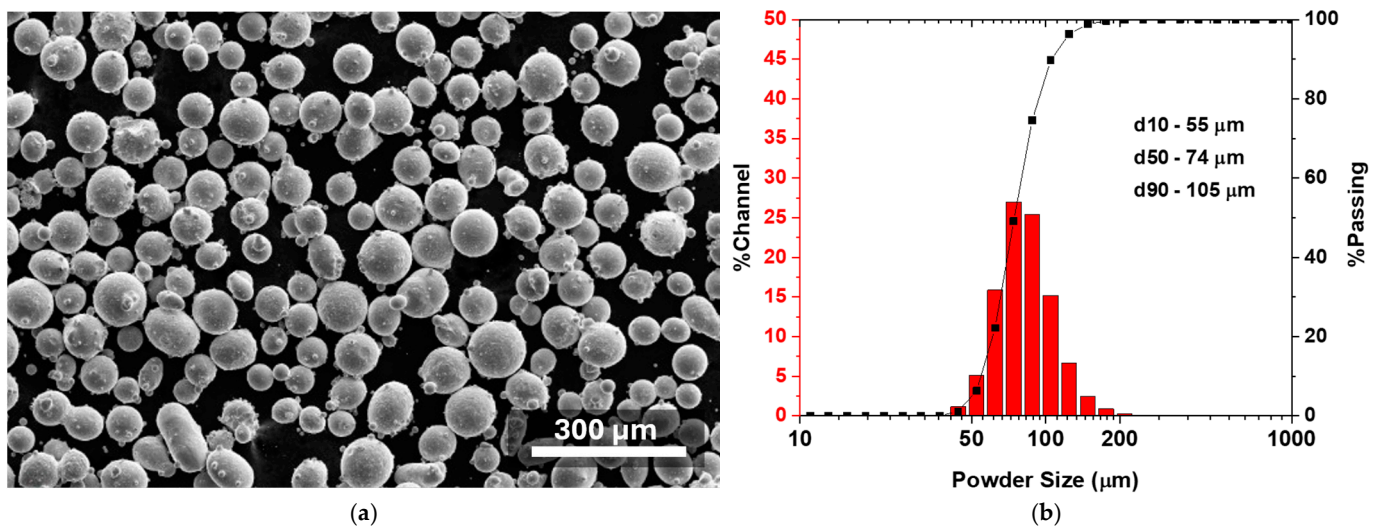
Figure 1. Precursor powder SS316 characteristics: (**a**) Micrograph of SS316L pre-alloyed powders showing spherical morphology; (**b**) Particle size distribution of powders used in EBM process.
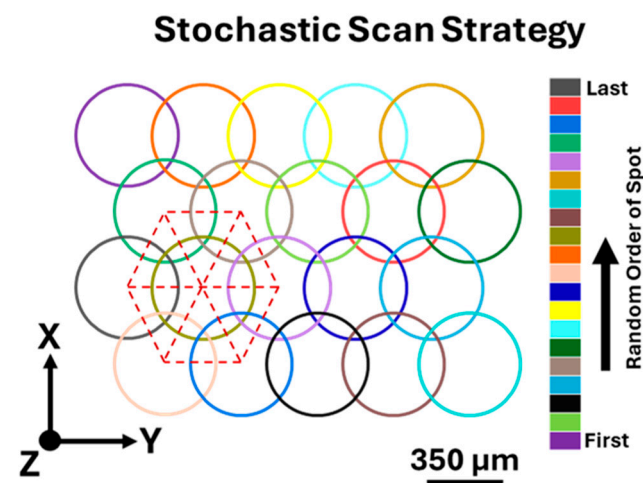
Figure 2. Stochastic scan strategy used in EBM of SS316L. Each circle represents a single spot melt region in a random spot order.

2.2. Microstructural and Mechanical Characterizations

The chemical composition of the SS316L material was measured using a Rigaku ZSX Primus IV WDXRF spectrometer (Rigaku Corporation, Tokyo, Japan) with 30 kV and 80 mA (Table 1). X-ray diffraction analysis was performed using a Rigaku Ultima III X-ray diffractometer (XRD, Rigaku Corporation, Tokyo, Japan) with monochromatic Cu Kα radiation,

operating at 35 kV and 28.6 mA. The data were collected with a scanning step of 0.02° and a scanning speed of 0.5°/min over the 2θ range of 35–100°. The metallographic analysis was carried out using the Keyence® VK-X1000 focus variation laser microscope (Keyence Corporation, Osaka, Japan) and Thermo Fisher Apreo 2C field emission scanning electron microscope (FESEM, Thermo Fisher Scientific, Waltham, MA, USA). The surface of a metallographic specimen was prepared by progressively polishing with emery papers ranging from P80 to P1200 grits, followed by fine polishing with a 0.25 μm diamond suspension on a Buehler TexMet™ cloth (Buehler International Inc., Lake Bluff, IL, USA). Subsequently, the samples were subjected to 24 h of vibratory polishing using a 0.06 μm colloidal silica suspension on a Buehler VibroMet™ 2 Vibratory Polisher (Buehler International Inc., Lake Bluff, IL, USA), with final gentle lapping in water on a Buehler ChemoMet™ cloth to remove any residual silica particles. The chemical analysis was performed using an EDAX Octane Elect Detector (EDAX, Inc., Mahwah, NJ, USA), and the crystallographic orientations (textures) were analyzed using an electron backscattered diffraction (EBSD, EDAX, Inc., Mahwah, NJ, USA) technique with an EDAX Velocity™ Detector, both equipped on the Thermo Fisher Apreo 2C FESEM. TSL OIM (orientation imaging microscopy) Analysis V8.6 (EDAX, Inc., Mahwah, NJ, USA) was used to analyze the EBSD data and calculate the orientation distribution functions. To observe the melt pool geometries, the surfaces of the material after polishing were chemically etched with a solution composed of 4% vol. HF and 8% vol. HNO_3 in distilled water at 293 K for 600 s [27]. Vickers microhardness measurements were performed on the components using a Buehler Wilson VH1162 hardness tester (Buehler International Inc., Lake Bluff, IL, USA) with a 200 g load and dwell time of 10 s. The tensile properties of the material at both room temperature and high temperature were investigated using a Plastometrex PLX-Benchtop system (Plastometrex Ltd., Cambridge, UK). This system employs a profilometry-based indentation plastometry (PIP) method, which includes inbuilt finite element modeling of the spherical indentation. A 1 mm radius spherical ball was used with a relatively larger load to create an indentation profile that converges on the best-fit set of plasticity parameters (in a constitutive law) to estimate the stress–strain behavior of a material [28,29]. Three spherical indentation measurements were performed at room temperature and at 773 K in the XZ plane of the component; the average mechanical properties are reported here.

Table 1. Chemical composition of the SS316L powders and EBM fabricated material.

Chemical Element (Wt. %)	Cr	Ni	Mo	Mn	Si	C	Fe
Powder	18	13	2.1	1.5	1.0	<0.03	Balance
SS316L Material	18.25	12.06	2.55	1.05	0.85	<0.03	Balance

2.3. Numerical Model

To gain fundamental insights into the thermo-kinetic and thermo-mechanical evolution during electron beam interaction and the evolution of associated microstructure and crystallographic texture, a 3D multiphysics finite element (FE) numerical model was developed for a single electron beam spot. Such insight/understanding can be obtained through computational-model-based thermo-kinetic and thermo-mechanical primary parameters: thermal gradient (*G*) and solidification rate (*R*) and secondary parameters: cooling rate (*G* × *R*) and morphology factor (*G/R*). The computational model was constructed based on the thermo-mechanical interactions observed in fusion-based additive manufacturing processes. In this approach, a bi-directionally coupled pure-conduction thermal model and a thermo-elastic-plastic mechanical model were solved simultaneously. The governing equation for conduction-based transient energy transfer was expressed as follows [30]:

$$\rho C_p \left(\frac{\partial T}{\partial t} + \vec{\nabla}.\left(\vec{u}\,T\right) \right) = \vec{\nabla} \cdot (k\vec{\nabla}T) + Q_V \tag{1}$$

where T is the temperature (K), ρ is the density $(\frac{kg}{m^3})$, k is the thermal conductivity $(\frac{W}{m \times K})$, C_p is the specific heat capacity $\left(\frac{J}{kg \times K}\right)$, Q_V $\left(\frac{W}{m^3}\right)$ is the absorbed heat, and $\vec{u}$ (m/s) is the advection velocity. Note that the term $\vec{u} = 0$, for the present case of pure conduction assumption. In terms of thermal boundary conditions, the electron-beam-illuminated top surface was prescribed with the following boundary condition:

$$-k\frac{\partial T}{\partial z} = -h_c[T - T_{amb}] - \epsilon\sigma_b\left[T^4 - T_{amb}^4\right] \tag{2}$$

where h_c is the convective heat transfer coefficient $(\frac{W}{m^2 K})$, ϵ is the emissivity, and σ_b is the Boltzmann constant $\left(\frac{J}{K}\right)$. In the computational domain, the non-irradiated boundary surfaces were prescribed with the following boundary condition:

$$-k\frac{\partial T}{\partial n} = -h_c[T - T_{amb}] \tag{3}$$

In the quasi-static mechanical model, the equilibrium in three dimensions was expressed as:

$$d\sigma_{ij,j} = 0 \tag{4}$$

Additionally, the elastic–plastic stress–strain relationship was defined as follows [31,32]:

$$d\varepsilon_{ij} = \left[\frac{1}{E}\left[-v\delta_{kl}\delta_{ij} + (1+v)\delta_{ik}\delta_{jl}\right] + d\lambda\frac{\partial f}{\partial \sigma_{ij}}\right]d\sigma_{kl} \tag{5}$$

where σ_{ij} and ε_{ij} are stress (Pa) and strain (m/m) tensors, respectively, v is the Poisson's ratio, δ is the Kronecker delta, and λ is the plastic potential (Pa). The mechanical model employed also followed a standard linear strain decomposition into elastic, plastic, and thermal strain, respectively, described by [33]:

$$d\varepsilon^{Total} = d\varepsilon^e + d\varepsilon^p + d\varepsilon^{th} \tag{6}$$

The thermal strain was represented as:

$$\varepsilon_{ij}^{th} = \alpha_{CTE}\delta_{ij}(T - T_{amb}) \tag{7}$$

where α_{CTE} is the coefficient of thermal expansion (1/K). As indicated in Equation (5), the yield function f in the model was approximated by an isotropic bilinear hardening model. Regarding the mechanical boundary conditions, the bottom surface of the substrate was constrained with a rigid support, while the remaining boundaries were left mechanically free.

In the Electron Beam-Powder Bed Fusion (EB-PBF) process, the material–heat source interaction was considered with the help of a volumetric heat source Q_V (Equation (1)) having a Gaussian heat distribution. In addition, the electron beam (EB) absorption and penetration in the bulk was realized using a penetration depth dependent analytical function as recommended by Lee et al. [24]. The mathematical formulation is expressed as follows:

$$Q_V = \alpha_e P_o \frac{f_s}{\pi d_b^2 D_p} exp\left[\frac{-f_s(x^2 + y^2)}{d_b^2}\right] \times \left[-3\left(\frac{z}{D_p}\right)^2 - 2\left(\frac{z}{D_p}\right) + 1\right] \tag{8}$$

In the above equation, α_e is the EB absorption factor taken to be 90%, f_s is the heat source spatial adjustment factor, and d_b is the EB diameter. In addition, the EB penetration depth D_p can be expressed as:

$$D_p = 2.1 \times 10^{-5}\left(\frac{V_e^2}{\rho_{bed}}\right)$$

The mathematical equations outlined above completed the thermal elastic–plastic formulation. As is common in the thermo-mechanical modeling of fusion-based AM processes, the powder bed was assumed to be a homogeneous continuum computational domain. The necessary thermo-physical properties and thermo-mechanical material model data were obtained from the literature [24,34–36], as mentioned in Table 2. Additionally, the powder bed porosity was incorporated using porosity-dependent scaling functions, as detailed in the author's previous work [31,32,37,38].

Table 2. EBM process and material parameters used for numerical modeling.

| Numerical Model Parameters	SS 316L
Liquidus temperature (T_l)	1733 K
Solidus temperature (T_s)	1693 K
Latent heat of fusion (L_m)	2.72×10^5 J kg^{-1}
Absorption factor (α_e)	0.9
Spatial adjustment factor (f_s)	2
E-beam voltage (V_e)	60 kV
Density solid phase (ρ_s)	7950 kg m^{-3}
Density liquid phase (ρ_l)	7380 kg m^{-3}
Poisson's ration (ν)	0.3
Emissivity (ϵ)	0.4
Convective heat transfer coefficient (h_c)	15 W m^{-2} K^{-1}
E-beam current (I)	11 mA
E-beam power (P_o)	660 W
E-beam interaction time/spot (τ)	0.25 ms
Powder bed packing density (ϕ)	0.55

The mathematical framework was solved using commercial finite element modeling (FEM) software COMSOL Multiphysics® V6.1. The conduction-based thermal model and the quasi-static thermal elastic–plastic mechanical model were solved using a bi-directionally coupled segregated solver. Meshing was performed with quadrilateral mapped elements, with a mesh size of 15 μm in the molten pool region and 50 μm in the regions distant from the melt pool. Computations were conducted on an Intel® Xeon® Gold 6252 CPU @ 2.10 GHz with 190 GB of RAM.

3. Results and Discussion

3.1. Microstructural Evolution

The X-ray diffraction measurement from the EBM fabricated SS316L material indicated the presence of a single austenitic phase after printing (Figure 3). As a first level of insight into the microstructure evolution, the etched surface on the XZ plane (parallel to the build direction) of the EBM-fabricated material revealed the presence of distinct melt pool boundaries. The melt pool overlap regions marked in Figure 4a are the regions where the material is partially re-melted. Also noticeable is the formation of cellular structures with varying morphology within the melt pool and melt pool overlap regions (Figure 4b). While the equiaxed cellular structures are present in the melt pool region, the elongated cells are predominantly observed within the melt pool overlap region. These microstructural features were influenced by the thermal gradients (G) and solidification rates (R) experienced during EBM fabrication with the stochastic beam scan strategy. The thermokinetic aspects associated with the present EBM processing of SS316L are discussed in detail in the following section. The high-magnification circular backscattered (CBS) electron images in Figure 4c–e revealed equiaxed and elongated cellular morphologies in the XZ plane of the component. The distinctly bright appearance of

the cellular boundaries is an indication of a segregation of the high atomic number elements in these regions compared to the cell interior (Z-contrast images). The EDS line scan across the cell boundaries identified a pronounced depletion of Fe, whereas there was a significant segregation of Mo and Si along the cell boundaries (Figure 5). Additionally, Cr, Ni, and Mn are also marginally enriched at the boundaries, although to a lesser extent than Mo and Si. In contrast, the cell cores are enriched with Fe (Figure 5). Such site-specific elemental segregation due to solute partitioning is characteristic of cellular solidification, where solute elements are rejected into the liquid phase and concentrated at the cell boundaries during rapid solidification [39,40]. Therefore, the distinct thermokinetic aspects affecting solidification during the stochastic spot e-beam process, as elaborated in the following section, are likely to have influenced solute segregation, resulting in enrichment at the cell boundaries.
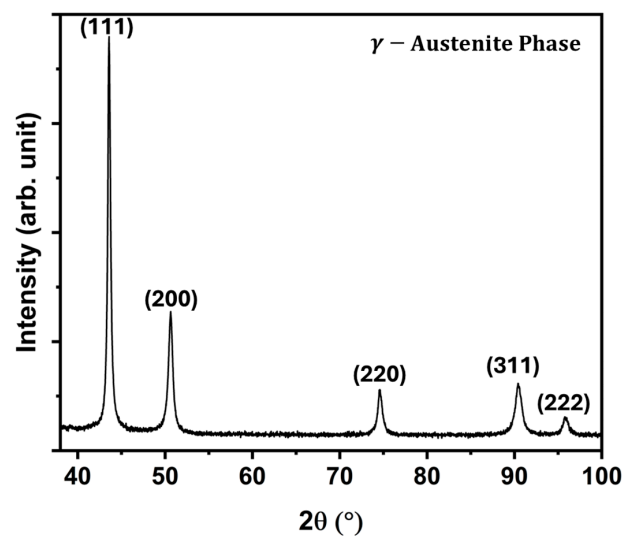
Figure 3. X-ray diffraction θ–2θ scan of the EBM fabricated SS316L showing the first five (hkl) peaks of the pure austenitic phase.
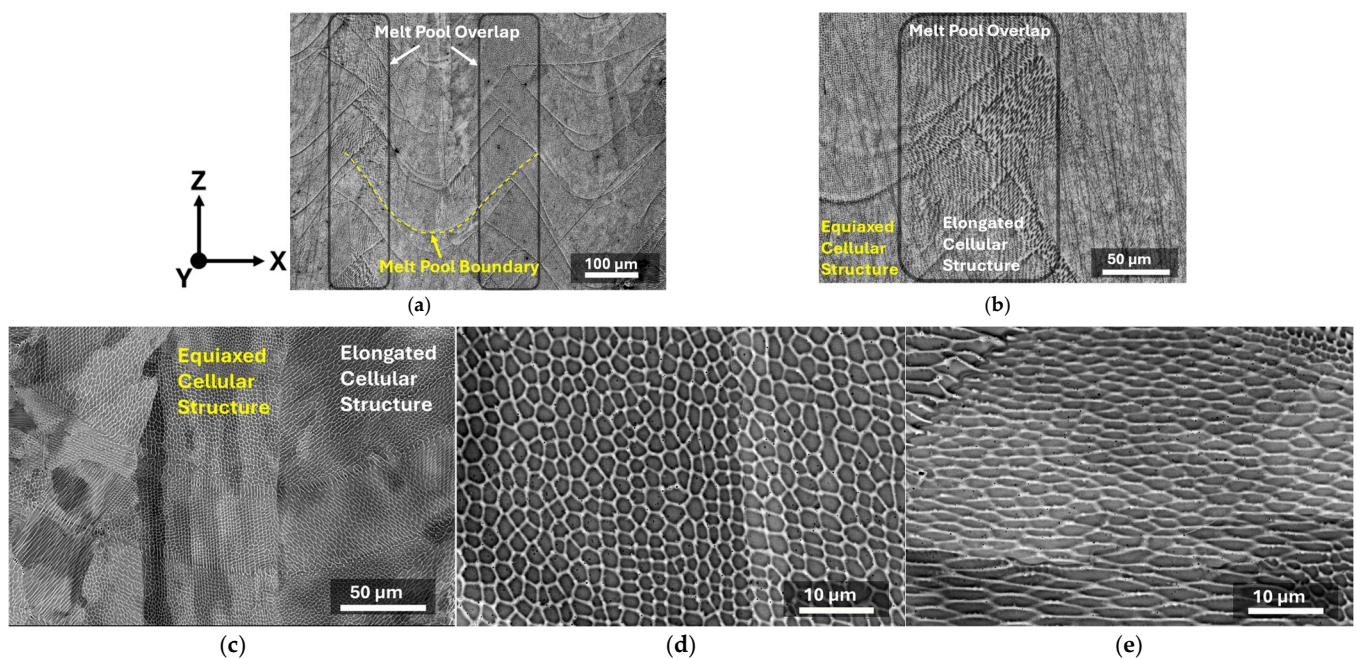
Figure 4. Optical micrographs of the cross-section parallel to the build direction (XZ-plane) showing: (**a**) Melt pool boundaries and melt pool overlap regions; (**b**) Contrast in cellular structure generation in these two regions. Circular backscattered (CBS) electron images showing: (**c**) Various cellular structures in the material (XZ-plane); (**d**) Equiaxed cellular structures; (**e**) Elongated cellular structures.
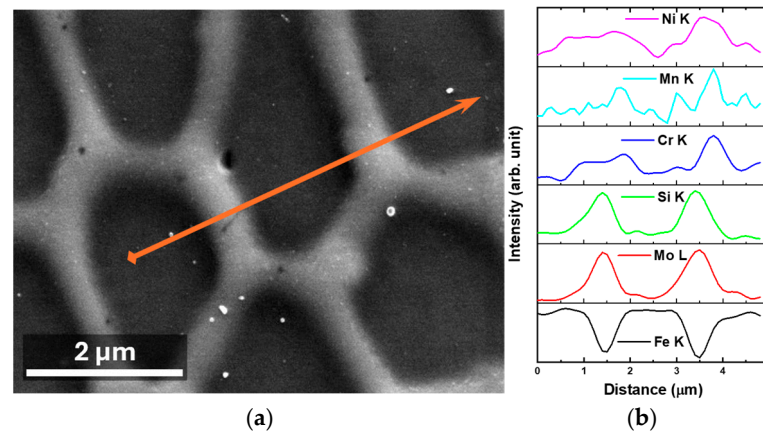
Figure 5. EDS line scan data showing microsegregation during EBM: (**a**) In the secondary electron image with a marked line; (**b**) Elemental distributions with corresponding element shells as a function of distance along the marked line.

3.2. Morphological and Crystallogic Texture Evolution Driven by Thermo-Kinetic Aspects

EBM fabrication with a stochastic scan strategy in conjunction with preheating is likely to generate distinct thermokinetic conditions that in turn drive evolution of the characteristic microstructure involving morphological and crystallographic textures in the material. Hence, as a preliminary effort, a numerical model discussed earlier in Section 2.3 was employed to computationally model the EBM process for a single spot interaction with the powder bed to understand the classic morphological and textural evolution. The stochastic spot melting strategy involves random ordering of the spot sequence at the temporal scale. Therefore, in the present case, the stochastic nature provides the newly melted region with sufficient cooling time before a new melting event takes place near the neighborhood (neighbor cool down approach FreeMelt®). Given that the beam interaction time for a single spot is 0.25 ms, it is highly unlikely that the newly melting region will experience a subsequent re-melting event resulting in a thermal gradient magnitude change at the solidification front (from the order of 10^7 K/m to a higher (10^8 or 10^9 K/m) or lower (10^5 or 10^4 K/m)). Further, during layer-by-layer printing, with the currently employed re-coater speed of 200 mm/s, the spreading and retraction of the re-coater over a 700 mm length build area approximately take ~7s. Therefore, a sufficient cool-off period exists between intralayer melting events. The preheating effect is already incorporated in the developed model with both an initial temperature and substrate top boundary temperature equilibrated at 1123 K before the e-beam spot interaction starts. Although actual EBM processing with a multi-spot stochastic scan strategy generates the microstructure influenced by multiple thermal cycles, the computationally predicted thermokinetic parameters for a single e-beam spot along the solidification front during the course of solidification provides an insight into the fundamentals of solidification (microstructure evolution) influenced by extremely dynamic thermokinetics of a single-spot EBM process which remains the foundation of the evolution of microstructure in e-beam processing with a multi-spot stochastic scanning. Nonetheless, separate efforts are being conducted by the present group to develop a physics-based multi-scale computational model of EBM processing with a multi-spot stochastic scanning strategy and will be reported in the future.

As reported in the literature, the evolution of thermokinetic parameters such as the thermal gradient (*G*) and solidification rate (*R*) along the solidification front can be utilized to qualitatively understand the solidified microstructure evolution during AM. More importantly, the grain morphology factor *G/R* and cooling rate $G \times R$ are prominently used to understand the grain morphology and its size. In light of this, in the current study, the changes in *G* and *R* were reported as a function of time along the OA line (X-direction) and OB line (Z-direction) within the e-beam melted region (Figure 6). Note that the values of *G*

and *R* were obtained at the solidification front, as it moves along the OA line (X-direction) and OB line (Z-direction) during the solidification process.


(a)

(b)

(c)

(d)
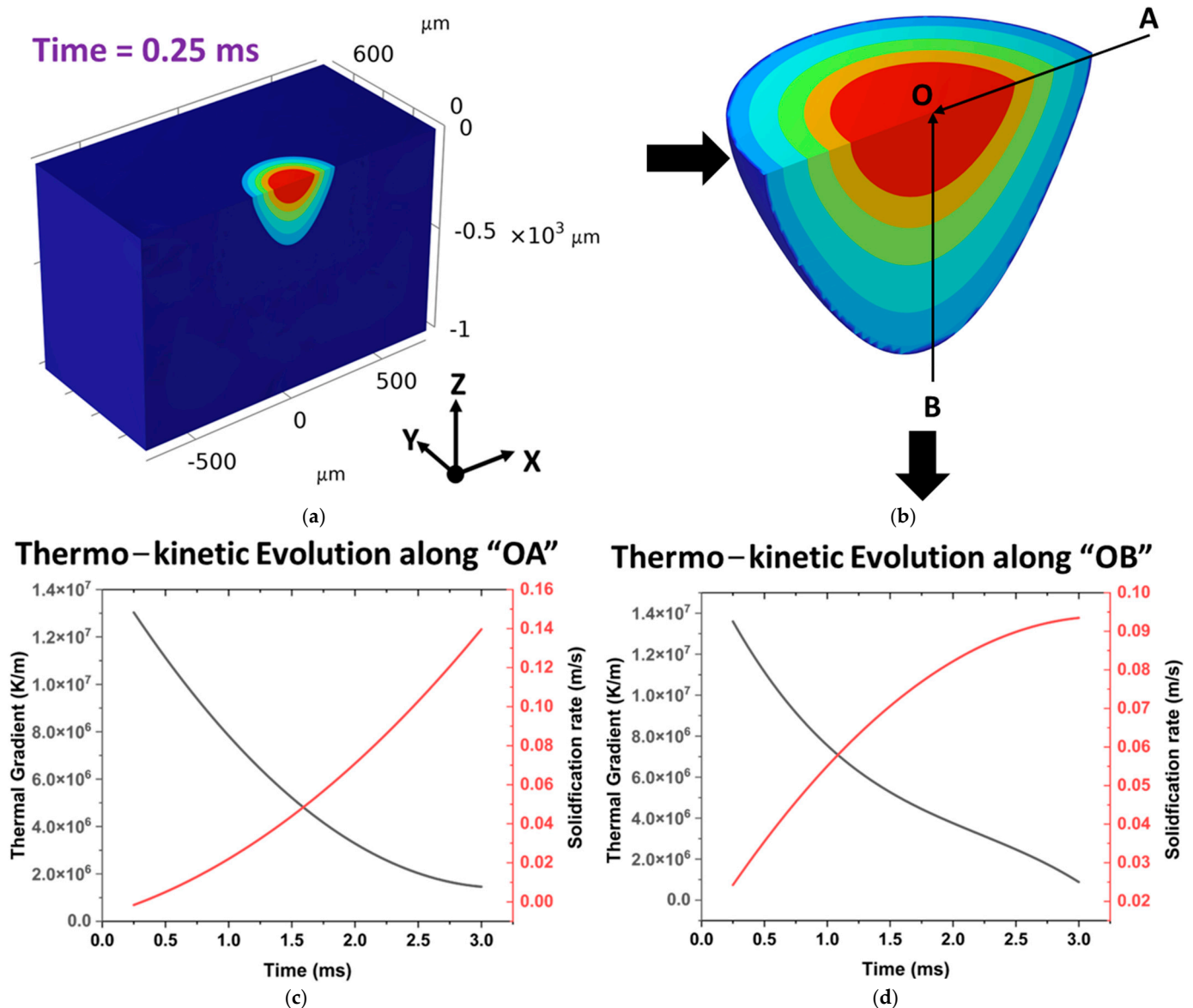
Figure 6. Thermal gradient and solidification rate as function of time along OA and OB lines in the melt pool: (**a**) Temperature distribution within the melt pool at 0.25 ms; (**b**) Schematic of melt pool and locations of OA and OB lines within the melt pool. Evolution of thermal gradient (*G*) and solidification rate (*R*) with time along the: (**c**) OA line; (**d**) OB line.

The thermal gradient observed along OA and OB within the melt pool are similar, 1.3×10^7 K/m at 0.25 ms (exactly after the dwell time of e-beam) and 1.0×10^6 K/m at 3 ms, respectively. The solidification rate along the OA line is increased to 0.14 m/s at 3 ms while it is 0.093 m/s along the OB line. The cooling rates ($G \times R$) of the order of 4.0×10^5 K/s are observed in the material from the proposed numerical model, which is typical of a fusion-based powder bed AM process [18,33]. The effects of the varying thermal gradients and solidification rates along the OA line and OB line on the microstructural evolution are discussed further.

The morphology of grains in the material visualized from the pseudo-3D EBSD representation revealed that the columnar grains were formed in the material along the build direction (Z) (Figure 7a). Notably, the columnar grains nucleated at the bottom of the build material were continuously grown up to the top of the build as depicted (Figure 7b). In

melting-based AM processes, the morphology of the grains is primarily influenced by the thermal gradient (G) and the solidification rate (R) at the solid–liquid interface of the solidifying melt pool. Due to the high cooling rates and rejection of solute at the solid–liquid interface, a compositional gradient is created, which causes constitutional undercooling of the liquid. This leads to instability at the solidification front, causing the morphology to transition from planar to different structures such as cellular, columnar dendritic, or equiaxed dendritic, depending on the G and R ratio. In the present study, the thermal gradient ranged from 1.3×10^7 K/m to 1.0×10^6 K/m, with a solidification rate between 0.005 to 0.14 m/s (Figure 6c,d). This combination of high thermal gradients and G/R ratio along the solidification front is typically likely to result in a columnar grain structure [41–43], due to the suppression of nucleation events facilitating equiaxed morphology under the current thermo-kinetic conditions [44]. Hence, the presence of preheating and a high thermal gradient continued during spot-by-spot remelting in the subsequent layers, resulted in a continuous growth of columnar grains, typical of the powder bed fusion process.

(**a**)   (**b**)   (**c**)
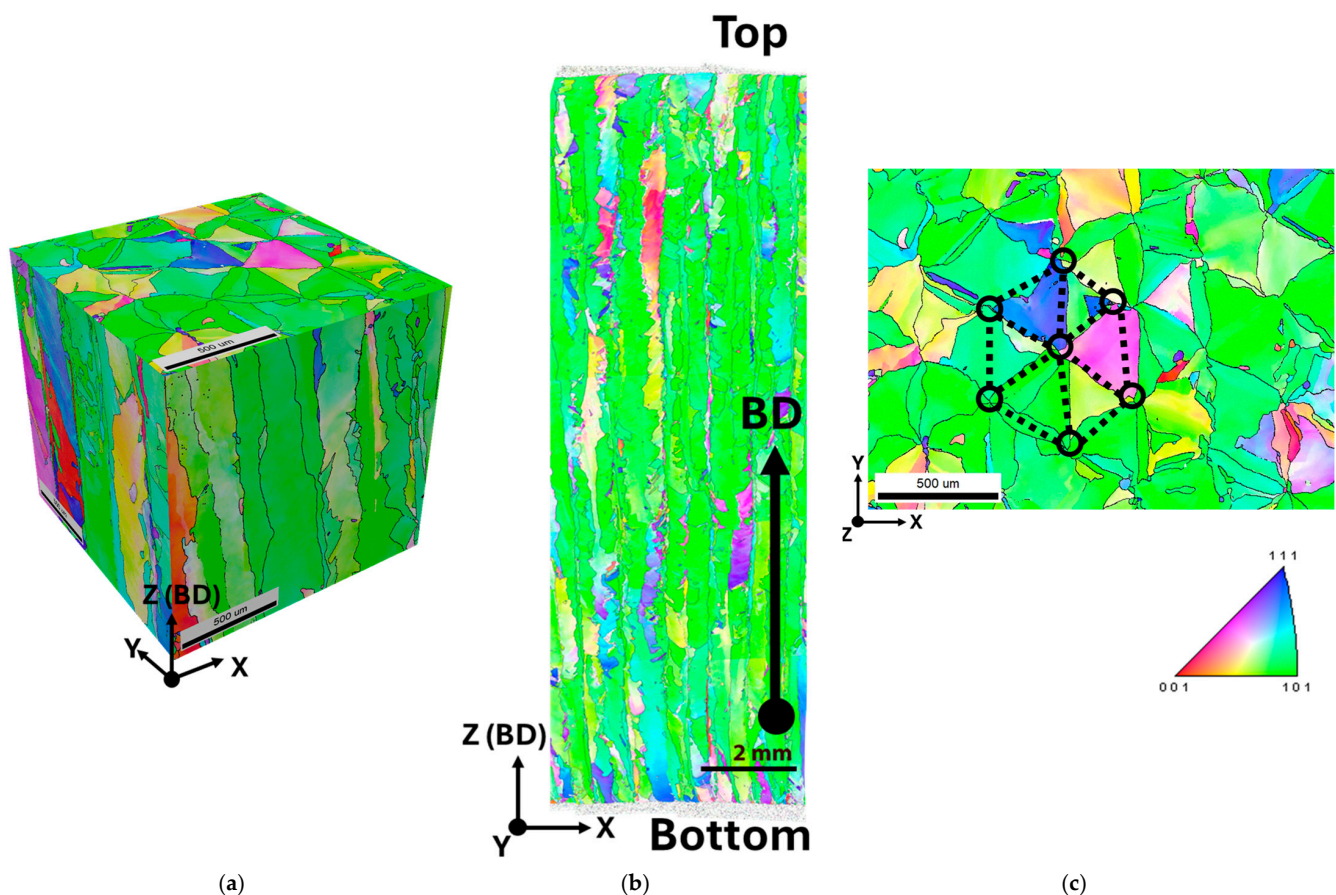
Figure 7. Inverse pole figure (IPF) maps of the EBM 3D-printed SS316L showing IPF-Z direction maps with black marked lines representing high angle grain boundaries: (**a**) A pseudo-3D EBSD representation of the build material; (**b**) IPF map of the cross-section (XZ-plane) parallel to the build direction (Z), revealing continuous columnar grains extending from the bottom to the top of the build; (**c**) IPF map of the build plane (XY-plane) showing the grain morphology with crystal directions.

The IPF-Z map of the XY plane (build plane) reveals that the grain morphology on the build plane has evolved into triangular shapes with junctions forming a hexagonal pattern (Figure 7c). Each location marked by the hollow black circle on the hexagonal pattern represents the center of the melt pool, which is the last region to solidify compared to the surrounding regions during the EBM process. This delayed solidification in such central regions leads to grain nucleation away from these locations, with subsequent grain growth extending outwards. At the boundaries between neighboring scan spots (marked with the

dotted line in Figure 7c), grains from different nucleation sites meet. Because the e-beam spots are arranged in a spatially hexagonal configuration as depicted earlier in a schematic of a stochastic e-beam scanning strategy of the EBM process (Figure 2), the common space within the centers of three neighboring e-beam spot melted zones forms a triangular shape where nucleation of grain occurs. Owing to the nature of the stochastic scanning pattern, the e-beam spots overlap with each other mimicking a spatial hexagonal pattern on the plane (XY) perpendicular to the build direction (Z). As a result of such spatially distributed overlapping melt pools, the remelting events also occur in a similar spatially distributed manner resulting in final solidified grains in a triangular morphology with hexagonal junctions. A similar observation of a hexagonal arrangement with a stochastic scan strategy has also been reported by Plotkowski et al. [45], albeit with a different material system. The color map in Figure 7b shows the inverse pole figure (IPF) map with a build direction (Z) majorly associated with a <110> crystallographic direction. It can be noticed that the grains in the bottom region of the build are majorly not oriented in any specific direction (random orientation). Though the IPF–BD is random at the bottom, there is a transition of the crystal directions towards the <110> crystallographic direction, with continued EBM fabrication via deposition of subsequent material layers; the rotation of the grains occurred in the subsequent layers. To clearly understand the mechanism of alignment in a preferred crystallographic direction, evolution of stress during EBM processing was investigated using the computational model (Figure 8).
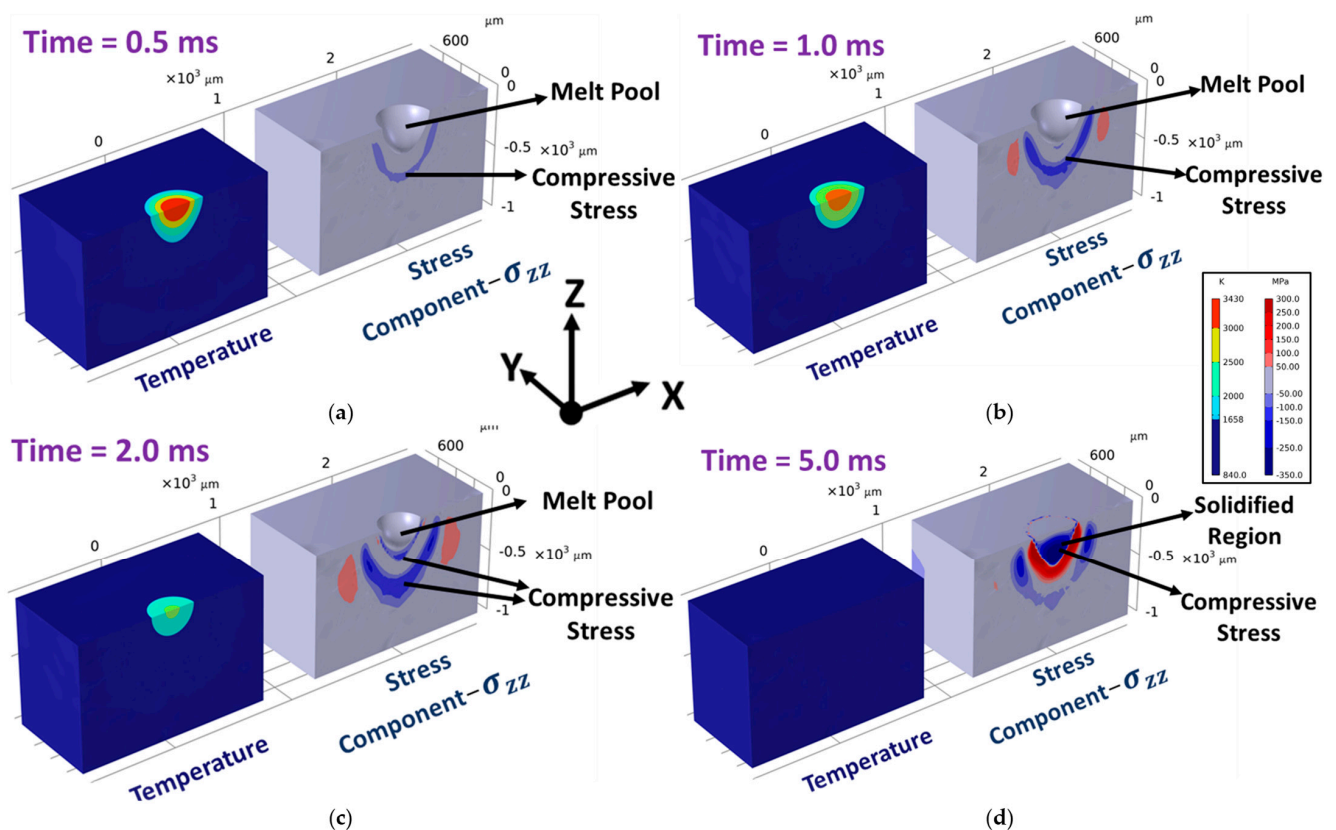

Figure 8. Computationally predicted melt pool characteristics of a single spot interaction showing temperature distribution (left) and stress distribution along the build direction (right) at time intervals of: (**a**) 0.5 ms; (**b**) 1.0 ms; (**c**) 2.0 ms; (**d**) 5.0 ms.

During the initial layers of the component fabrication, heat dissipation was relatively uniform, and nucleation sites (locations where new grains form during solidification) occurred randomly. This leads to random grain orientation at the bottom of the build. As the deposition progresses, the thermal gradients (G) along the build direction (Z) became slower from 1.3×10^7 K/m to 1.0×10^6 K/m (Figure 6c). Furthermore, the

heat was conducted from newly deposited top layers to earlier deposited bottom layers thereby inducing a growth in a preferred crystallographic direction within the grains. FCC metals experiencing extremely rapid cooling rates during solidification generate grains with the growth directions along the fastest growth rate in the crystallographic direction of the lowest atomic density (<001>), whereas the growth is slowest in the densest crystallographic directions [46]. However, even though the current EBM process experienced an average rapid cooling of 4.0×10^5 K/s with layer-by-layer printing with a powder bed temperature of 1123 K, the columnar grains were grown along the <110> crystallographic direction which was parallel to the build direction (Z). Such a contrast can be attributed to development of stresses during solidification in the material. When the FCC material experiences compression, grains rotate toward the <110> direction. This occurs because, under compressive loading, the crystal structure aligns itself to activate multiple slip systems that ease deformation and accommodate plastic strain more effectively [47]. In EBM processed SS316L of the current work, stress evolution within the melt pool during the transformation from liquid to solid at different time scales are computationally predicted (Figure 8). It is evident from these computational predictions that primarily the compressive stresses were developed in the solidified region. It should be noted that, once the met pool is solidified, the region below the melt pool experienced tensile stresses (Figure 8d) due to contraction of the solidified region (i.e., temperature gradient mechanism under thermal loading [30]). However, the magnitude of compressive stresses evolved within the solidified region being very high (of the order of 350 MPa) led rotation of randomly oriented grains at the bottom of the build towards the <110>, which was also the direction parallel to the build direction. During successive EBM layer printings, the induced compressive stresses in the layers below would be relieved with the tensile stress generation as depicted in Figure 8d for the region below the solidified region. In addition to the generation of compressive stress controlling the texture formation, some studies reported the solidification dynamics, crystallographic symmetry, and use of a compatible scan patterns may also partially play a role in the texture formation in fusion-based AM [45,48–50]. The higher solidification kinetics favors the <001> direction along Z, while the growth of <011> along Z is expected to be formed when the geometry of the melt pool becomes short and wide [48]. Furthermore, previous studies reported the observation of grains with <110>||Z in the melt pool overlap regions while <001>||Z within the melt pool regions in SS316L; it is attributed to the solidification dynamics and the direction of the misorientation thermal gradients in the melt pool overlap regions [45,49,50]. While in the present study, the generation of grains having <110>||Z within the melt pool rather than <001>||Z suggests that the compressive stress generation is mainly influencing the texture formation. Pistor et al. reported a similar mechanism of thermo-mechanically induced texture formation during additive manufacturing to generate single metallic crystals [47].

The above-described phenomenon can be further confirmed by earlier visual observations of the IPF map (Figure 7b) showing the <110> crystallographic directions of the grains were parallel to the build direction of the component, suggesting the formation of a fiber texture along the build direction. Furthermore, the (001), (110), and (111) pole figures show the presence of corresponding poles forming a circle along the build direction (Z) as shown with dashed black circles in Figure 9a. The discrete intensities along the dashed black circles suggest that there was a strong texture evolution with poles parallel to the X-direction in addition to (110) poles parallel to the build direction. To identify orientations belonging to these intensities, the orientation distribution function (ODF) $\varphi2 = 45°$ section was calculated and is presented in Figure 9b. It is noticeable that there are two strong intensities along the $\Phi = 90°$, which belong to {110} <111> and {110} <001> orientations. The correlated misorientation angle distribution of the grains with respect to uncorrelated misorientation angle distribution in the microstructure shows higher intensity at 55°, which is the misorientation angle between these two {110} <111> and {110} <001> strong orientations in the material in addition to the low angle grain boundaries (< 15°) of similar orientations.

Pole Figures

ODF
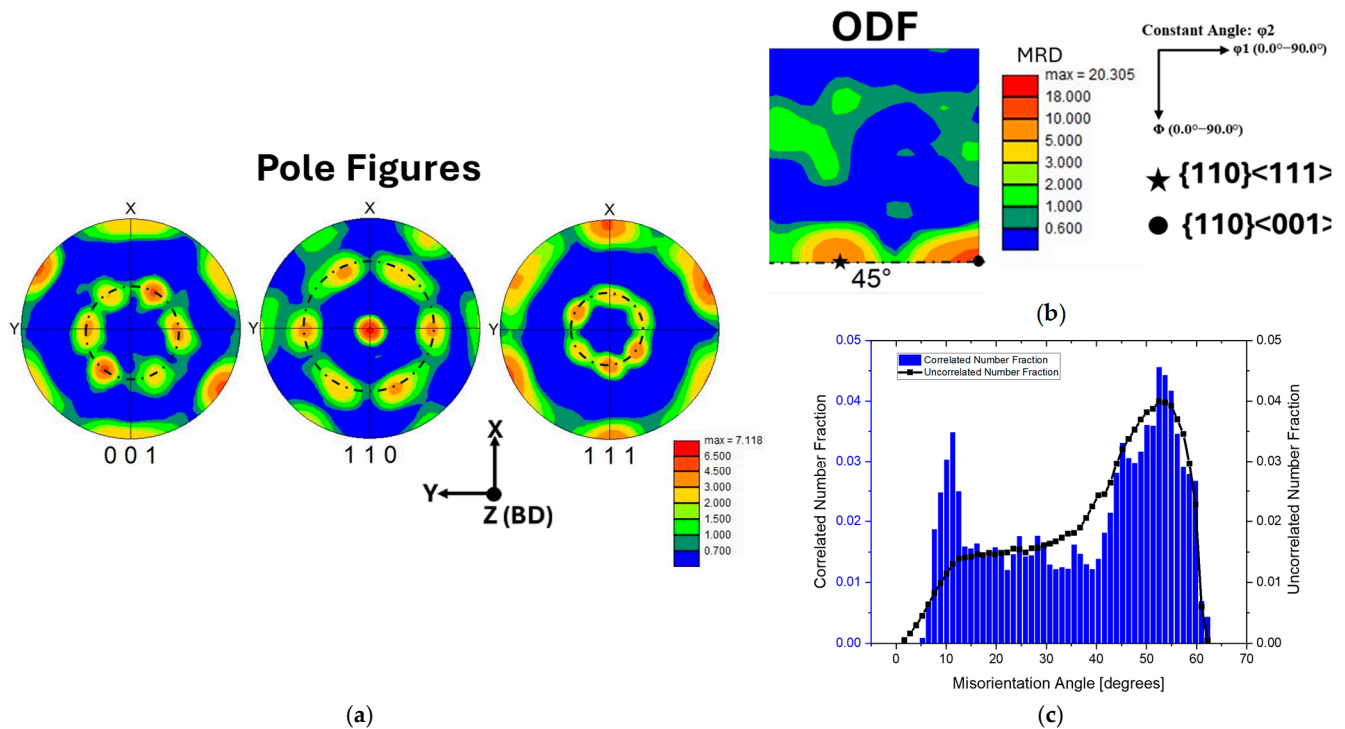
Figure 9. (a) Pole figures of (001), (110), and (111) planes, showing a strong {110}∥ build direction (Z) fiber texture; **(b)** Orientation distribution function section at φ2 = 45°, showing formation of {110}<111> and {110}<001> crystal orientations in the material; **(c)** Correlated and uncorrelated misorientation angle distributions of the material.

The volume fraction of {110}<001> grains is higher than that of {110}<111>, as indicated by the larger multiples of random distribution (MRD) of 17 in the orientation distribution function (ODF) at φ2 = 45° (Figure 9b), suggesting a higher number of grains with <001> crystal direction along X-direction than <111> crystal direction. Though the thermal gradients were similar along both X (OA line) and Z (OB line) directions within the melt pool (Figure 6c), the solidification rate along the X-direction (OA line) (0.14 m/s at 3 ms) was nearly one and half times higher than that observed in the Z-direction (OB line) (0.093 m/s at 3 ms). It is clear that the presence of compressive stress along the build direction (Z) led to a rotation of grains towards <110> crystallographic direction (Figure 8). Additionally, these observed slower solidification rates along the build direction (Z) (0.093 m/s at 3 ms) reduced the chances of the formation of grains with the <001> crystallographic direction along the build direction (Z). Furthermore, the grains became aligned along the X-direction ∥<001>, as it is the faster growth direction due to its lower atomic density [46], which supports enhanced solidification kinetics (0.14 m/s at 3 ms). Along the X-direction, the tensile stress would also be generated due to Poisson's effect during solidification, in response to the compressive stresses evolving in the Z-direction. The stress in the X-direction is Poisson's ratio (0.3 for SS316L) times the magnitude of compressive stress in the Z-direction (350 MPa) (Figure 8d). Although the magnitude of stress along the X-direction (tensile, 105 MPa) was comparatively lower, it could still contribute to the formation of grains with <111> crystallographic directions along the X-direction to accommodate tensile residual stresses due to the lower energy required for deformation [51–53]. The formation of grains having component X-directions along <001>, <111> crystallographic directions also suggests that there are still some directional variations in grain growth rates due to localized thermal gradients. Although stochastic scanning randomizes the temporal order of e-beam spots, the spatial arrangement of the e-beam spot might lead to some preferential thermo-kinetics-driven crystallographic growth. As depicted in Figure 2, the arrangement of spots in the X-direction and Y-direction is not similar (hexagonal arrangement); hence,

the melt pool overlap regions in between two neighboring spots would be oriented at approximately 90° and 30° to the X-direction (red dashed lines as marked in Figure 2) and could lead to preferential alignment of <001> and <111> crystallographic directions parallel to the X-direction, respectively [54]. It is also possible that these grains with orientations other than <001>||X may also be facilitated by small random fluctuations or perturbations in either the microstructure or melting process [48]. The regions having decreased solidification rates could possibly lead to the formation of the other orientation with the crystal direction <111> || X-direction.

3.3. Mechanical Properties

Vickers hardness of the SS316L material was measured to be 170 ± 2 HV. The stress–strain curves generated from spherical indentation tests at room temperature (RT) and 773 K, highlight significant differences in mechanical behavior (Figure 10). The SS316L material in this study exhibited the yield strength (σ_y) of 184 MPa, similar to conventionally processed ASM SS316L material, but lower than other AM processed materials [55], primarily due to coarser grains and a higher proportion of low-angle grain boundaries (fraction of 0.19, Figure 9c), which offer less resistance to the initiation of dislocation motion. Nevertheless, the ultimate tensile strength (σ_u) of 544 MPa remains comparable to both conventionally and AM processed materials. This is likely because the cellular structures typically formed in additively manufactured materials impede dislocation motion, thereby enhancing the ultimate tensile strength with resistance at higher stresses [56–59]. Despite the reduction in strength at elevated temperatures, the material exhibits noticeable strain hardening at 773 K with a higher strain due to increased atomic mobility allowing for easier dislocation movement and recovery processes. The scanning strategy could considerably influence the microstructure and mechanical properties [60] while the use of a stochastic scanning strategy enhances the strength of a component [61]. Additionally, the continuation of strain hardening at elevated temperatures suggests that the material maintains its work-hardening ability, which can be beneficial for high-temperature applications where a balance between strength and ductility is required.

Properties	RT	773 K
σ_y (MPa)	184 ± 36	114 ± 21
σ_u (MPa)	544 ± 22	330 ± 25
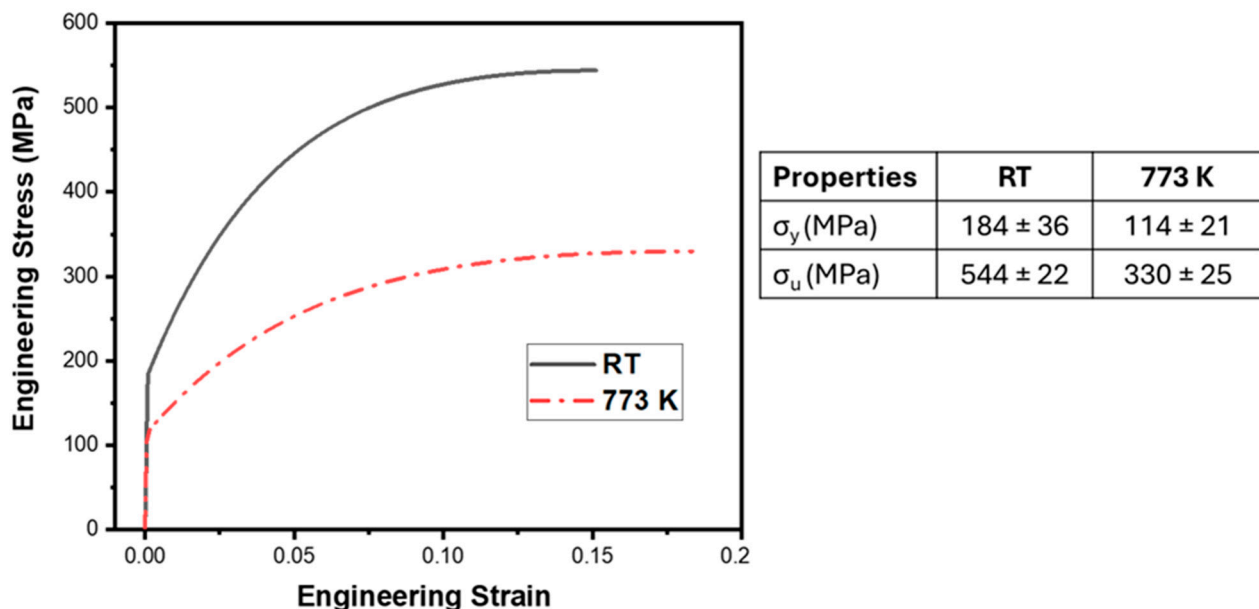
Figure 10. Stress–strain curves estimated from the profilometry-based spherical indentation plastometry of the SS316L material at room temperature (RT) and 773 K.

Overall, the current study provides a fundamental investigation of the complex interplay of thermo-kinetic and thermo-mechanical phenomena on the evolution of grain morphology and texture using a stochastic e-beam spot scanning strategy at a preheat

temperature of 1123 K. However, the evolution of a thermal gradient in the case of multiple spot overlap and layer-by-layer thermal accumulation requires further numerical analysis to better understand the thermo-kinetics-driven microstructural evolution. Nevertheless, the current study provides a fundamental basis for further exploration of physics-informed pathways to unravel the process–structure response of such a complex scanning strategy to the EBM process.

4. Conclusions

From the material characterization complemented with computational modeling and mechanical testing of the EBM-fabricated SS316L material, using a stochastic scan strategy and preheat temperature of 1123K, the following conclusions were drawn in this study:

(1) The understanding of thermokinetic and thermomechanical aspects of the EBM process corroborated the microstructural evolution and texture formation in SS316L, resulting in continuous columnar grains aligned with the <110> direction along the build direction.

(2) The preferred orientations of {110}<001> and {110}<111> formed in the material were mainly driven by the solidification rate kinetics and stress evolution within the melt pool.

(3) The spatial arrangement of the stochastic scan significantly influenced the grain morphology in the build plane, resulting in the formation of triangular-shaped grains within the plane orthogonal to the build direction.

(4) The mechanical behavior of the EBM-fabricated SS316L material, particularly the work-hardening behavior observed at elevated temperatures, makes it suitable for high-temperature applications, offering a balance between strength and ductility.

Author Contributions: Conceptualization, K.N.C.K., S.S., M.R. and N.B.D.; Data curation, K.N.C.K., M.R., R.R., K.K.V., S.D. and Z.W.H.; Formal analysis, S.S., M.R., R.R. and K.K.V.; Funding acquisition, N.B.D.; Investigation, K.N.C.K., S.S., M.R. and N.B.D.; Methodology, K.N.C.K., S.S., M.R., S.D., Z.W.H., R.B. and N.B.D.; Project administration, N.B.D.; Resources, N.B.D.; Software, K.N.C.K. and S.S.; Supervision, N.B.D.; Validation, K.N.C.K., S.S., M.R. and N.B.D.; Visualization, K.N.C.K., S.S. and N.B.D.; Writing—original draft, K.N.C.K. and S.S.; Writing—review and editing, R.B. and N.B.D. All authors have read and agreed to the published version of the manuscript.

Data Availability Statement: The data that support the findings of this study are available on request from the corresponding author.

Conflicts of Interest: The authors declare no conflicts of interest.

References

1. Ford, S.; Despeisse, M. Additive Manufacturing and Sustainability: An Exploratory Study of the Advantages and Challenges. *J. Clean. Prod.* **2016**, *137*, 1573–1587. [CrossRef]
2. Oros Daraban, A.E.; Negrea, C.S.; Artimon, F.G.P.; Angelescu, D.; Popan, G.; Gheorghe, S.I.; Gheorghe, M. A Deep Look at Metal Additive Manufacturing Recycling and Use Tools for Sustainability Performance. *Sustainability* **2019**, *11*, 5494. [CrossRef]
3. Galati, M.; Calignano, F.; Viccica, M.; Iuliano, L. Additive Manufacturing Redesigning of Metallic Parts for High Precision Machines. *Crystals* **2020**, *10*, 161. [CrossRef]
4. Hegab, H.; Khanna, N.; Monib, N.; Salem, A. Design for Sustainable Additive Manufacturing: A Review. *Sustain. Mater. Technol.* **2023**, *35*, e00576. [CrossRef]
5. Zhang, L.-C.; Liu, Y.; Li, S.; Hao, Y. Additive Manufacturing of Titanium Alloys by Electron Beam Melting: A Review. *Adv. Eng. Mater.* **2018**, *20*, 1700842. [CrossRef]
6. Kolamroudi, M.K.; Asmael, M.; Ilkan, M.; Kordani, N. Developments on Electron Beam Melting (EBM) of Ti–6Al–4V: A Review. *Trans. Indian Inst. Met.* **2021**, *74*, 783–790. [CrossRef]

7.   Zhang, L.; Zhai, W.; Zhou, W.; Chen, X.; Chen, L.; Han, B.; Cao, L.; Bi, G. Improvement of Mechanical Properties through Inhibition of Oxidation by Adding TiC Particles in Laser Aided Additive Manufacturing of Stainless Steel 316L. *Mater. Sci. Eng. A* **2022**, *853*, 143767. [CrossRef]

8.   Zhao, X.; Wei, Y.; Mansour, R.; Dadbakhsh, S.; Rashid, A. Effect of Scanning Strategy on Thermal Stresses and Strains during Electron Beam Melting of Inconel 625: Experiment and Simulation. *Materials* **2023**, *16*, 443. [CrossRef]

9.   Carpenter, K.; Tabei, A. On Residual Stress Development, Prevention, and Compensation in Metal Additive Manufacturing. *Materials* **2020**, *13*, 255. [CrossRef]

10.   Shih, C.-C.; Shih, C.-M.; Su, Y.-Y.; Su, L.H.J.; Chang, M.-S.; Lin, S.-J. Effect of Surface Oxide Properties on Corrosion Resistance of 316L Stainless Steel for Biomedical Applications. *Corros. Sci.* **2004**, *46*, 427–441. [CrossRef]

11.   Desu, R.K.; Nitin Krishnamurthy, H.; Balu, A.; Gupta, A.K.; Singh, S.K. Mechanical Properties of Austenitic Stainless Steel 304L and 316L at Elevated Temperatures. *J. Mater. Res. Technol.* **2016**, *5*, 13–20. [CrossRef]

12.   Lo, K.H.; Shek, C.H.; Lai, J.K.L. Recent Developments in Stainless Steels. *Mater. Sci. Eng. R Rep.* **2009**, *65*, 39–104. [CrossRef]

13.   Baddoo, N.R. Stainless Steel in Construction: A Review of Research, Applications, Challenges and Opportunities. *J. Constr. Steel Res.* **2008**, *64*, 1199–1206. [CrossRef]

14.   Wang, D.; Zhao, D.; Liang, X.; Li, X.; Lin, F. Multiple Stages of Smoking Phenomenon in Electron Beam Powder Bed Fusion Process. *Addit. Manuf.* **2023**, *66*, 103434. [CrossRef]

15.   Cordero, Z.C.; Meyer, H.M.; Nandwana, P.; Dehoff, R.R. Powder Bed Charging during Electron-Beam Additive Manufacturing. *Acta Mater* **2017**, *124*, 437–445. [CrossRef]

16.   Ali, H.; Ma, L.; Ghadbeigi, H.; Mumtaz, K. In-Situ Residual Stress Reduction, Martensitic Decomposition and Mechanical Properties Enhancement through High Temperature Powder Bed Pre-Heating of Selective Laser Melted Ti6Al4V. *Mater. Sci. Eng. A* **2017**, *695*, 211–220. [CrossRef]

17.   Wensrich, C.M.; Luzin, V.; Hendriks, J.N.; Pant, P.; Gregg, A.W.T. Residual Stress in Additively Manufactured Inconel Cubes; Selective Laser Melting versus Electron Beam Melting and a Comparison of Modelling Techniques. *Mater. Des.* **2024**, *244*, 113108. [CrossRef]

18.   Körner, C. Additive Manufacturing of Metallic Components by Selective Electron Beam Melting—A Review. *Int. Mater. Rev.* **2016**, *61*, 361–377. [CrossRef]

19.   Sames, W.J.; List, F.A.; Pannala, S.; Dehoff, R.R.; Babu, S.S. The Metallurgy and Processing Science of Metal Additive Manufacturing. *Int. Mater. Rev.* **2016**, *61*, 315–360. [CrossRef]

20.   Sames, W.J.; Unocic, K.A.; Dehoff, R.R.; Lolla, T.; Babu, S.S. Thermal Effects on Microstructural Heterogeneity of Inconel 718 Materials Fabricated by Electron Beam Melting. *J. Mater. Res.* **2014**, *29*, 1920–1930. [CrossRef]

21.   Xing, L.-L.; Zhang, W.-J.; Zhao, C.-C.; Gao, W.-Q.; Shen, Z.-J.; Liu, W. Influence of Powder Bed Temperature on the Microstructure and Mechanical Properties of Ti-6Al-4V Alloy Fabricated via Laser Powder Bed Fusion. *Materials* **2021**, *14*, 2278. [CrossRef]

22.   Shao, M.; Vijayan, S.; Nandwana, P.; Jinschek, J.R. The Effect of Beam Scan Strategies on Microstructural Variations in Ti-6Al-4V Fabricated by Electron Beam Powder Bed Fusion. *Mater. Des.* **2020**, *196*, 109165. [CrossRef]

23.   Raghavan, N.; Simunovic, S.; Dehoff, R.; Plotkowski, A.; Turner, J.; Kirka, M.; Babu, S. Localized Melt-Scan Strategy for Site Specific Control of Grain Size and Primary Dendrite Arm Spacing in Electron Beam Additive Manufacturing. *Acta Mater.* **2017**, *140*, 375–387. [CrossRef]

24.   Lee, Y.S.; Kirka, M.M.; Dinwiddie, R.B.; Raghavan, N.; Turner, J.; Dehoff, R.R.; Babu, S.S. Role of Scan Strategies on Thermal Gradient and Solidification Rate in Electron Beam Powder Bed Fusion. *Addit. Manuf.* **2018**, *22*, 516–527. [CrossRef]

25.   Nandwana, P.; Lee, Y. Influence of Scan Strategy on Porosity and Microstructure of Ti-6Al-4V Fabricated by Electron Beam Powder Bed Fusion. *Mater. Today Commun.* **2020**, *24*, 100962. [CrossRef]

26.   Ren, X.; Peng, H.; Li, J.; Liu, H.; Huang, L.; Yi, X. Selective Electron Beam Melting (SEBM) of Pure Tungsten: Metallurgical Defects, Microstructure, Texture and Mechanical Properties. *Materials* **2022**, *15*, 1172. [CrossRef] [PubMed]

27.   Scherillo, F.; Manco, E.; Hassanin, A.E.; Franchitti, S.; Pirozzi, C.; Borrelli, R. Chemical Surface Finishing of Electron Beam Melted Ti6Al4V Using HF-HNO3 Solutions. *J. Manuf. Process.* **2020**, *60*, 400–409. [CrossRef]

28.   Campbell, J.E.; Zhang, H.; Burley, M.; Gee, M.; Fry, A.T.; Dean, J.; Clyne, T.W. A Critical Appraisal of the Instrumented Indentation Technique and Profilometry-Based Inverse Finite Element Method Indentation Plastometry for Obtaining Stress–Strain Curves. *Adv. Eng. Mater.* **2021**, *23*, 2001496. [CrossRef]

29.   Clyne, T.W.; Campbell, J.E.; Burley, M.; Dean, J. Profilometry-Based Inverse Finite Element Method Indentation Plastometry. *Adv. Eng. Mater.* **2021**, *23*, 2100437. [CrossRef]

30.   Sharma, S.; Joshi, S.S.; Pantawane, M.V.; Radhakrishnan, M.; Mazumder, S.; Dahotre, N.B. Multiphysics Multi-Scale Computational Framework for Linking Process–Structure–Property Relationships in Metal Additive Manufacturing: A Critical Review. *Int. Mater. Rev.* **2023**, *68*, 943–1009. [CrossRef]

31.   Pantawane, M.V.; Sharma, S.; Sharma, A.; Dasari, S.; Banerjee, S.; Banerjee, R.; Dahotre, N.B. Coarsening of Martensite with Multiple Generations of Twins in Laser Additively Manufactured Ti6Al4V. *Acta Mater.* **2021**, *213*, 116954. [CrossRef]

32.   Sharma, S.; Krishna, K.V.M.; Joshi, S.S.; Radhakrishnan, M.; Palaniappan, S.; Dussa, S.; Banerjee, R.; Dahotre, N.B. Laser Based Additive Manufacturing of Tungsten: Multi-Scale Thermo-Kinetic and Thermo-Mechanical Computational Model and Experiments. *Acta Mater.* **2023**, *259*, 119244. [CrossRef]

33. Dahotre, N.B.; Pantawane, M.V.; Sharma, S. *Laser-Based Additive Manufacturing: Modeling, Simulation, and Experiments*; John Wiley & Sons: Hoboken, NJ, USA, 2022.

34. Nain, V.; Engel, T.; Carin, M.; Boisselier, D. Conventional Meso-Scale and Time-Efficient Sub-Track-Scale Thermomechanical Model for Directed Energy Deposition. *Materials* **2022**, *15*, 4093. [CrossRef]

35. Biegler, M.; Graf, B.; Rethmeier, M. In-Situ Distortions in LMD Additive Manufacturing Walls Can Be Measured with Digital Image Correlation and Predicted Using Numerical Simulations. *Addit. Manuf.* **2018**, *20*, 101–110. [CrossRef]

36. Mukherjee, T.; Wei, H.L.; De, A.; DebRoy, T. Heat and Fluid Flow in Additive Manufacturing—Part II: Powder Bed Fusion of Stainless Steel, and Titanium, Nickel and Aluminum Base Alloys. *Comput. Mater. Sci.* **2018**, *150*, 369–380. [CrossRef]

37. Joshi, S.S.; Sharma, S.; Mazumder, S.; Pantawane, M.V.; Dahotre, N.B. Solidification and Microstructure Evolution in Additively Manufactured H13 Steel via Directed Energy Deposition: Integrated Experimental and Computational Approach. *J. Manuf. Process.* **2021**, *68*, 852–866. [CrossRef]

38. Mazumder, S.; Pantawane, M.V.; Patil, S.M.; Radhakrishnan, M.; Sharma, S.; McKinstry, M.; Dahotre, N.B. Thermokinetically Driven Microstructural Evolution in Laser-Based Directed Energy-Deposited CoCrMo Biomedical Alloy. *Adv. Eng. Mater.* **2022**, *24*, 2200352. [CrossRef]

39. Birnbaum, A.J.; Steuben, J.C.; Barrick, E.J.; Iliopoulos, A.P.; Michopoulos, J.G. Intrinsic Strain Aging, Σ3 Boundaries, and Origins of Cellular Substructure in Additively Manufactured 316L. *Addit. Manuf.* **2019**, *29*, 100784. [CrossRef]

40. Inoue, H.; Koseki, T.; Okita, S.; Fuji, M. Solidification and Transformation Behaviour of Austenitic Stainless Steel Weld Metals Solidified as Primary Austenite: Study of Solidification and Subsequent Transformation of Cr-Ni Stainless Steel Weld Metals (1st Report). *Weld. Int.* **1997**, *11*, 876–887. [CrossRef]

41. Kiran, A.; Koukolíková, M.; Vavřík, J.; Urbánek, M.; Džugan, J. Base Plate Preheating Effect on Microstructure of 316L Stainless Steel Single Track Deposition by Directed Energy Deposition. *Materials* **2021**, *14*, 5129. [CrossRef]

42. Hunt, J.D. Steady State Columnar and Equiaxed Growth of Dendrites and Eutectic. *Mater. Sci. Eng.* **1984**, *65*, 75–83. [CrossRef]

43. Liu, Y.; Shi, J. Epitaxial Growth and Stray Grain Control toward Single-Crystal Metallic Materials by Additive Manufacturing: A Review. *Adv. Eng. Mater.* **2023**, *25*, 2201917. [CrossRef]

44. Prasad, A.; Yuan, L.; Lee, P.; Patel, M.; Qiu, D.; Easton, M.; StJohn, D. Towards Understanding Grain Nucleation under Additive Manufacturing Solidification Conditions. *Acta Mater.* **2020**, *195*, 392–403. [CrossRef]

45. Plotkowski, A.; Ferguson, J.; Stump, B.; Halsey, W.; Paquit, V.; Joslin, C.; Babu, S.S.; Marquez Rossy, A.; Kirka, M.M.; Dehoff, R.R. A Stochastic Scan Strategy for Grain Structure Control in Complex Geometries Using Electron Beam Powder Bed Fusion. *Addit. Manuf.* **2021**, *46*, 102092. [CrossRef]

46. Chattopadhyay, C.; Sangal, S.; Mondal, K. A Relook at the Preferred Growth Direction of the Solid–Liquid Interface during Solidification of Pure Metals. *Acta Mater.* **2010**, *58*, 5342–5353. [CrossRef]

47. Pistor, J.; Körner, C. A Novel Mechanism to Generate Metallic Single Crystals. *Sci. Rep.* **2021**, *11*, 24482. [CrossRef]

48. Fernandez-Zelaia, P.; Kirka, M.M.; Rossy, A.M.; Lee, Y.; Dryepondt, S.N. Nickel-Based Superalloy Single Crystals Fabricated via Electron Beam Melting. *Acta Mater.* **2021**, *216*, 117133. [CrossRef]

49. Zinovieva, O.; Zinoviev, A.; Romanova, V.; Balokhonov, R. Three-Dimensional Analysis of Grain Structure and Texture of Additively Manufactured 316L Austenitic Stainless Steel. *Addit. Manuf.* **2020**, *36*, 101521. [CrossRef]

50. Helmer, H.; Bauereiß, A.; Singer, R.F.; Körner, C. Grain Structure Evolution in Inconel 718 during Selective Electron Beam Melting. *Mater. Sci. Eng. A* **2016**, *668*, 180–187. [CrossRef]

51. Güden, M.; Yavaş, H.; Tanrıkulu, A.A.; Taşdemirci, A.; Akın, B.; Enser, S.; Karakuş, A.; Hamat, B.A. Orientation Dependent Tensile Properties of a Selective-Laser-Melt 316L Stainless Steel. *Mater. Sci. Eng. A* **2021**, *824*, 141808. [CrossRef]

52. Wang, X.; Muñiz-Lerma, J.A.; Attarian Shandiz, M.; Sanchez-Mata, O.; Brochu, M. Crystallographic-Orientation-Dependent Tensile Behaviours of Stainless Steel 316L Fabricated by Laser Powder Bed Fusion. *Mater. Sci. Eng. A* **2019**, *766*, 138395. [CrossRef]

53. Wang, X.; Muñiz-Lerma, J.A.; Sanchez-Mata, O.; Attarian Shandiz, M.; Brodusch, N.; Gauvin, R.; Brochu, M. Characterization of Single Crystalline Austenitic Stainless Steel Thin Struts Processed by Laser Powder Bed Fusion. *Scr. Mater.* **2019**, *163*, 51–56. [CrossRef]

54. Andreau, O.; Koutiri, I.; Peyre, P.; Penot, J.-D.; Saintier, N.; Pessard, E.; De Terris, T.; Dupuy, C.; Baudin, T. Texture Control of 316L Parts by Modulation of the Melt Pool Morphology in Selective Laser Melting. *J. Mater. Process. Technol.* **2019**, *264*, 21–31. [CrossRef]

55. Sumanariu, C.A.; Amza, C.G.; Baciu, F.; Vasile, M.I.; Nicoara, A.I. Comparative Analysis of Mechanical Properties: Conventional vs. Additive Manufacturing for Stainless Steel 316L. *Materials* **2024**, *17*, 4808. [CrossRef] [PubMed]

56. Voisin, T.; Forien, J.-B.; Perron, A.; Aubry, S.; Bertin, N.; Samanta, A.; Baker, A.; Wang, Y.M. New Insights on Cellular Structures Strengthening Mechanisms and Thermal Stability of an Austenitic Stainless Steel Fabricated by Laser Powder-Bed-Fusion. *Acta Mater.* **2021**, *203*, 116476. [CrossRef]

57. Wang, Y.M.; Voisin, T.; McKeown, J.T.; Ye, J.; Calta, N.P.; Li, Z.; Zeng, Z.; Zhang, Y.; Chen, W.; Roehling, T.T.; et al. Additively Manufactured Hierarchical Stainless Steels with High Strength and Ductility. *Nat. Mater.* **2018**, *17*, 63–71. [CrossRef]

58. Kim, J.-M.; Jin, H.-H.; Kwon, J.; Kang, S.H.; Lee, B.-S. Effects of Cellular Segregation for High Strength and Ductility of Additively Manufactured 304L Stainless Steel. *Mater. Charact.* **2022**, *194*, 112364. [CrossRef]

59. Deng, P.; Yin, H.; Song, M.; Li, D.; Zheng, Y.; Prorok, B.C.; Lou, X. On the Thermal Stability of Dislocation Cellular Structures in Additively Manufactured Austenitic Stainless Steels: Roles of Heavy Element Segregation and Stacking Fault Energy. *JOM* **2020**, *72*, 4232–4243. [CrossRef]

60. Salman, O.O.; Brenne, F.; Niendorf, T.; Eckert, J.; Prashanth, K.G.; He, T.; Scudino, S. Impact of the Scanning Strategy on the Mechanical Behavior of 316L Steel Synthesized by Selective Laser Melting. *J. Manuf. Process.* **2019**, *45*, 255–261. [CrossRef]

61. Ghouse, S.; Babu, S.; Van Arkel, R.J.; Nai, K.; Hooper, P.A.; Jeffers, J.R.T. The Influence of Laser Parameters and Scanning Strategies on the Mechanical Properties of a Stochastic Porous Material. *Mater. Des.* **2017**, *131*, 498–508. [CrossRef]